

Accepted Manuscript

Enhanced photocatalytic activities of g-C₃N₄ with large specific surface area via a facile one-step synthesis process

Deqiang Feng, Yahui Cheng, Jie He, Lingcheng Zheng, Dawei Shao, Weichao Wang, Weihua Wang, Feng Lu, Hong Dong, Hui Liu, Rongkun Zheng, Hui Liu

PII: S0008-6223(17)30959-4

DOI: [10.1016/j.carbon.2017.09.084](https://doi.org/10.1016/j.carbon.2017.09.084)

Reference: CARBON 12414

To appear in: *Carbon*

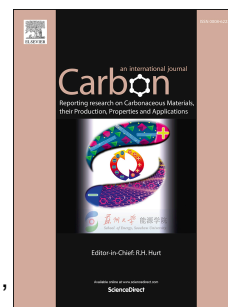
Received Date: 7 July 2017

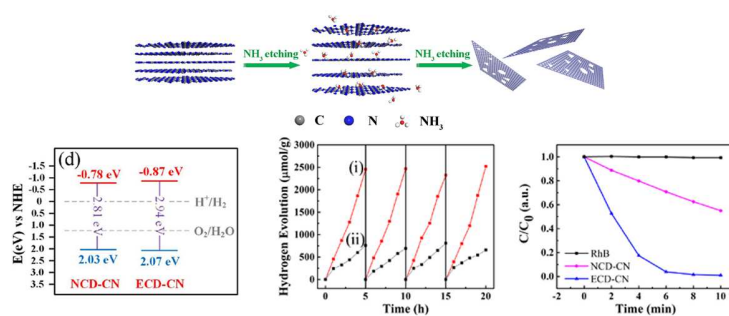
Revised Date: 13 September 2017

Accepted Date: 21 September 2017

Please cite this article as: D. Feng, Y. Cheng, J. He, L. Zheng, D. Shao, W. Wang, W. Wang, F. Lu, H. Dong, H. Liu, R. Zheng, H. Liu, Enhanced photocatalytic activities of g-C₃N₄ with large specific surface area via a facile one-step synthesis process, *Carbon* (2017), doi: 10.1016/j.carbon.2017.09.084.

This is a PDF file of an unedited manuscript that has been accepted for publication. As a service to our customers we are providing this early version of the manuscript. The manuscript will undergo copyediting, typesetting, and review of the resulting proof before it is published in its final form. Please note that during the production process errors may be discovered which could affect the content, and all legal disclaimers that apply to the journal pertain.





Enhanced photocatalytic activities of g-C₃N₄ with large specific surface area via a facile one-step synthesis process

Deqiang Feng,^a Yahui Cheng,^{a,b,*} Jie He,^a Lingcheng Zheng,^a Dawei Shao,^a Weichao Wang,^a Weihua Wang,^a Feng Lu,^a Hong Dong,^a Hui Liu,^b Rongkun Zheng^c and Hui Liu^a

^a *Department of Electronics and Key Laboratory of Photo-Electronic Thin Film Devices and Technology of Tianjin, Nankai University, Tianjin 300350, China*

^b *Research Group of Quantum-Dot Materials & Devices, Institute of New-Energy Materials, Tianjin University, Tianjin 300350, China*

^c *School of Physics, The University of Sydney, NSW 2006, Australia*

* Corresponding Author.

E-mail address: chengyahui@nankai.edu.cn (Y. H. Cheng)

ABSTRACT

Graphitic carbon nitride (g-C₃N₄) has been considered as a promising metal-free catalyst for a wide range of application due to its intriguing properties. However, the photocatalytic performance is restricted by the small specific surface area (SSA) and limited active sites. Here, a facile one-step method was employed to prepare thin porous g-C₃N₄ with large SSA by condensation of urea. During the pyrolysis process, the self-generated NH₃ not only participates in the condensation reaction to obtain bulk g-C₃N₄, but also etches crystal lattice to form thinner nanosheets. A high SSA of 141.4 m² g⁻¹ for the sample synthesized in the enclosed condition (ECD-CN) is obtained, which is much larger than the SSA of 57.4 m² g⁻¹ for the sample synthesized in the non-enclosed condition (NCD-CN). These porous nanosheets with the enhanced SSA endow g-C₃N₄ more exposed active sites and shorten the carrier diffusion length. As a result, the ECD-CN sample exhibits much higher photodegradation rate on rhodamine B (99.0% within 10 min) and hydrogen evolution rate (504.2 μmol h⁻¹ g⁻¹) under visible-light. This study provides a facile and template-free strategy in preparing efficient, sustainable and visible-light-driven photocatalyst.

1. Introduction

Since the discovery of photocatalytic water splitting on TiO_2 photoelectrode by Fujishima *et al.* in 1972 [1], semiconductor photocatalysis utilizing clean and sustainable solar energy has been employed widely as a “green” technology [2-5]. Among the numerous types of photocatalysts, metal-free graphitic carbon nitride ($\text{g-C}_3\text{N}_4$) has attracted tremendous attention. The $\text{g-C}_3\text{N}_4$ is a two-dimensional layered polymer semiconductor with tri-s-triazine connected with planar amino groups in each layer and weak van der Waals force between layers. The unique structure of $\text{g-C}_3\text{N}_4$ gives it many excellent physicochemical characteristics, such as thermodynamic and chemical stability, abundant and low-cost building elements, environmental friendliness, and especially, a suitable electronic structure with band edges straddling the water redox potentials for the efficient photocatalytic reactions [6-8]. However, the photocatalytic performance of $\text{g-C}_3\text{N}_4$ is still restricted by the drawbacks of high recombination rate of photogenerated electron-hole pairs and limited active sites [9,10]. Frequently, preparation of photocatalyst with large specific surface area (SSA) is considered to be an effective strategy to improve the photocatalytic performance by providing abundant active sites to promote the redox reaction and reducing the carriers transport distance [11,12].

The SSA of $\text{g-C}_3\text{N}_4$ could theoretically reach $2500 \text{ m}^2 \text{ g}^{-1}$ for the perfect monolayer $\text{g-C}_3\text{N}_4$ [13]. However, usually it can only be dozens of or even below $10 \text{ m}^2 \text{ g}^{-1}$ due to the stacking of polymeric nanosheets. To date, plenty of preparation methods have been developed to obtain $\text{g-C}_3\text{N}_4$ with larger SSA. In principle, these methods can be

classified into two categories. One category is modulating the morphology (porous nanostructure, hollow spheres, 1-dimension nanostructures, etc.) of g-C₃N₄ by template assisted method [14-18]. Normally, the template can be the hard-template such as anodic aluminium oxide (AAO) [16], silica [19-21], TiO₂ [22], or organic molecules soft-template such as Pluronic P123 [23] and thiourea [24]. The SSA of g-C₃N₄ obtained by template methods can reach several hundreds of m² g⁻¹. For instance, mesoporous g-C₃N₄ has been synthesized by using silica nanoparticles as a hard template, and the SSA is up to 373 m² g⁻¹ [11]. By employing SBA-15, a kind of hexagonally ordered mesoporous silica, as a hard template, the SSA can be as high as 239 m² g⁻¹ [25]. However, this category involves to the introduction and removal of the template. Another category is top-down chemical or thermal exfoliation of bulk g-C₃N₄ [26-30]. Recently, ammonia molecules were found to etch bulk g-C₃N₄ during post thermal treatment process which resulted in the formation of porous and ultrathin g-C₃N₄ nanosheets. For instance, Liang *et al.* heated the bulk g-C₃N₄ in NH₃ atmosphere to prepare holey g-C₃N₄ nanosheets [28]. They proposed that during the reaction with NH₃, bulk g-C₃N₄ gradually decomposes into gaseous products and the released gas assists the expansion of the stacked g-C₃N₄ layers, thereby resulting in the formation of few-layer holey nanosheets with SSA of 196 m² g⁻¹, which is 32.6 times larger than that of bulk g-C₃N₄. The hydrogen production rate of these holey g-C₃N₄ nanosheets is 20 times higher than that of the bulk g-C₃N₄. In another work, Yang *et al.* also obtained porous g-C₃N₄ by heating the bulk counterpart in NH₃ atmosphere [31]. The porous sample displays a large SSA of 149 m² g⁻¹. However, all

of the above-mentioned methods need additional post-treatment processes. Obviously, a simple, direct and template-free strategy to synthesize g-C₃N₄ with large SSA is desired.

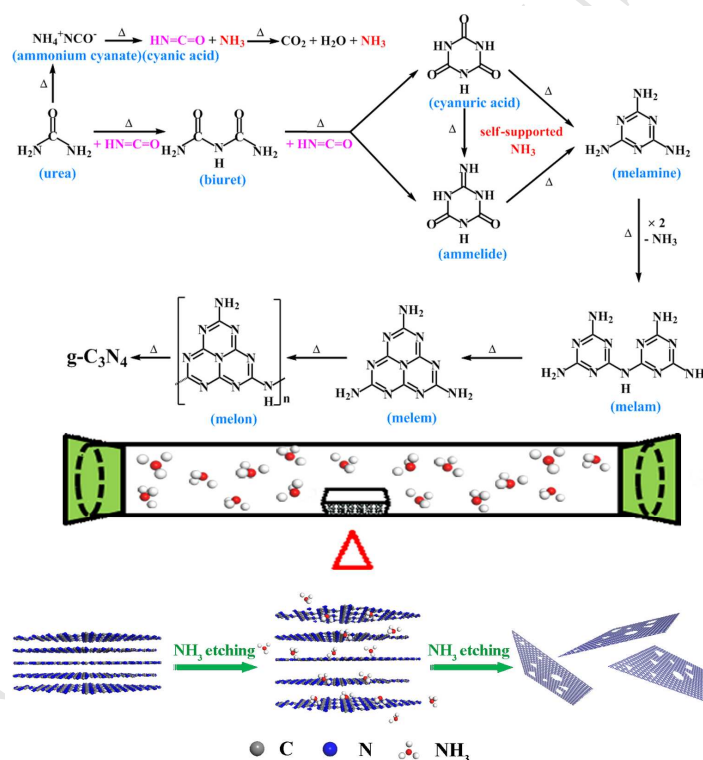
Inspired by the use of NH₃ post-treatment in the preparation of porous and ultrathin g-C₃N₄, in this work we tried to prepare g-C₃N₄ with large SSA by one-step method without passing over any etching gas. It is known that urea is a sort of nitrogen-rich organic precursor, which can release massive NH₃ during the thermal condensation process to form g-C₃N₄ (Schematic 1) [32]. According to the above information, we proposed a facile method to synthesize g-C₃N₄ with large SSA by utilizing the pyrolysis-generated NH₃ from urea under an enclosed condition. On one hand, the released-NH₃ participates in the condensation reaction to obtain bulk g-C₃N₄ [32], and on the other hand, the redundant NH₃ etches the crystal lattice to form the thinner nanosheets with high SSA. The largest SSA of the obtained g-C₃N₄ is up to 141.4 m² g⁻¹, which has significantly improved the photodegradation performance of rhodamine B (RhB) and the H₂ evolution rate.

2. Experimental section

2.1. Preparation of g-C₃N₄ samples

All chemicals were analytical grade and used without further purification. The g-C₃N₄ samples were synthesized by a facile one-step thermal treatment of urea precursor. Typically, a certain amount (for instance 10 g) of urea in a 20 mL crucible with a cover was put in a tubular furnace and heated at 550 °C for 4 h under enclosed ambient condition by keeping two perovskite plugs being inserted in both ends of the

quartz tube as shown in Schematic 1. It should be noted here that although the ends of the tube were blocked, they were not completely sealed to prevent explosion. The heating rate was $2.5\text{ }^{\circ}\text{C min}^{-1}$. After cooling down to room temperature, the g- C_3N_4 samples were gained and denoted as ECD-CN. For the comparative analysis, the sample synthesized under non-enclosed condition without plugging the ends of quartz tube was denoted as NCD-CN. Also, melamine and dicyandiamide (DCDA) were used as precursors to synthesize bulk g- C_3N_4 by the general method [33,34], and the samples were denoted as M-CN and D-CN, respectively.



Schematic 1. The proposed reaction mechanism for the pyrolysis of urea into g- C_3N_4 under enclosed condition.

2.2. Characterization

The microstructure of samples was observed by transmission electron microscopy (TEM, JEOL JEM-2010 FEF) operating at 200 kV. The thickness of nanosheets was

characterized by atomic force microscopy (AFM, Agilent afm5500). Crystal structure was examined using X-ray diffraction (XRD, Rigaku mini FlexII) with Cu K α radiation ($\lambda = 0.15406$ nm) at a scanning rate of 2 °/min. X-ray photoelectron spectroscopy (XPS) measurements were carried out on a Thermo Escalab 250Xi spectrometer equipped with Al K α X-ray source. Nitrogen adsorption-desorption isotherms were obtained on a specific surface & pore size analyzer (BeiShiDe Instrument, 3H-2000PM2) with all samples being degassed at 200 °C for 5 h prior to the measurements. The special surface areas of samples were calculated by the Brunauer-Emmett-Teller (BET) method at a relative pressure range of $p/p_0 = 0.03-0.35$, and pore size distributions were calculated according to the Barrett-Joyner-Halenda (BJH) method. Fourier transform infrared spectroscopy (FT-IR, Bruker Tensor 37) was measured using KBr pallets. UV-vis absorption spectra were obtained on an UV-vis spectrophotometer (UV-2600, Shimadzu) equipped with an integrating sphere assembly.

2.3. Photoelectrochemical measurement

Photoelectrochemical (PEC) test was carried out on an electrochemical workstation (PAP versastat 4-200) in a standard three-electrode model with Pt wire as the counter electrode and Ag/AgCl (3.5 M KCl) as the reference electrode. To prepare a working electrode, g-C₃N₄ samples synthesized under different conditions were deposited on a 10×10 mm² fluorine-doped tin oxide (FTO) substrate. 0.1 M Na₂SO₄ was used as the electrolyte and a 300 W Xe-arc lamp equipped with wavelength cutoff filter ($\lambda > 400$ nm) was utilized as the light source. The frequency of electrochemical

impedance spectroscopy (EIS) was ranged from 100 mHz to 100 kHz with the alternating current signal amplitude of 10 mV.

2.4. Photocatalytic activity measurements

Photocatalytic activities of NCD-CN and ECD-CN samples were investigated by degradation of aqueous RhB under visible-light. In detail, 10 mg of photocatalyst was dispersed in 60 mL of RhB aqueous solution (10 mg L^{-1}) in a double-deck quartz reactor with circulating water cooling system to keep a constant temperature. Prior to irradiation, the suspension was magnetically stirred for 60 min in the dark to ensure absorption-desorption equilibrium on the photocatalyst surface. The light source is a 300 W Xe-arc lamp equipped with 400 nm cutoff filter. At certain time intervals, 4 mL of solution was sampled and centrifuged to remove the photocatalyst. Then the supernatant was extracted and measured on UV-vis spectrophotometer. Degradation efficiency of RhB was evaluated by recording variations of the absorption band maximum (553 nm). The removal ratio was calculated as $\eta = (C_0 - C) / C_0 \times 100\% = (A_0 - A) / A_0 \times 100\%$, where C_0 and A_0 are the initial concentration and absorbency of RhB respectively, and C and A are the revised concentration and absorbency respectively after irradiation.

In addition, the photocatalytic performance was also characterized by the water splitting for hydrogen evolution under visible-light. Typically, 50 mg of photocatalyst was dispersed in 50 mL of deionized water. Then 10 v/v % triethanolamine (TEOA) was added serving as sacrificial electron donor and 2 wt % H_2PtCl_6 aqueous solution was added as the precursor of cocatalyst Pt that was in-situ photoreduced during the

photocatalytic reaction. Afterwards, the solution was degassed with Ar for 30 min to completely remove the air and subsequently sealed carefully. At last, the solution was irradiated under a 300 W Xe-arc lamp equipped with cutoff filter ($\lambda > 400$ nm). The photocatalytic H₂ evolution rate was determined using an offline gas chromatograph (GC Smart GC-2018, Shimadzu).

3. Results and discussion

3.1. Structure and morphology

Crystalline structures of g-C₃N₄ for NCD-CN and ECD-CN samples are examined by two feature signals on the XRD patterns. In Fig. 1a, the minor (100) peak relates to the in-plane repeated tri-s-triazine units while the main peak (002) corresponds to the inter-layer stacking of the conjugated aromatic CN units [32]. As displayed in the magnified XRD patterns in Fig. 1b and 1c, compared with NCD-CN, ECD-CN shows an upshift of 0.3 ° of 2θ for the (002) peak and a downshift of 0.4 ° for the (100) peak. According to the Bragg equation, $2d \sin \theta = \lambda$, these shifts indicate that there are evident in-plane extended distortion and inter-layer compressed distortion for the ECD-CN sample. The inter-layer compressed distortion suggests that the distance between each two layers, i.e., (002) planes spacing, is small, so the conjugated aromatic system becomes denser, leading to an enhanced structural connection via enhanced van der Waals interaction between layers [35]. Such an enhanced connection will result in a stronger overlap of molecular orbits of aromatic sheet stacks, which subsequently alters the band gap of g-C₃N₄ [36]. What's more, the smaller full width at half maximum (FWHM) of the ECD-CN sample than that of

NCD-CN sample indicates a better crystallinity of ECD-CN. For comparison, XRD patterns of D-CN and M-CN are displayed in Fig. S1. Clearly, two characteristic diffraction peaks corresponding to the (002) plane and (100) plane were observed, indicating that g-C₃N₄s were synthesized successfully using different precursors. Compared with D-CN and M-CN, ECD-CN still shows an upshift of 0.1 ° of 2θ for the (002) peak, suggesting that ECD-CN has smaller interlayer distance than the samples synthesized by the general method.

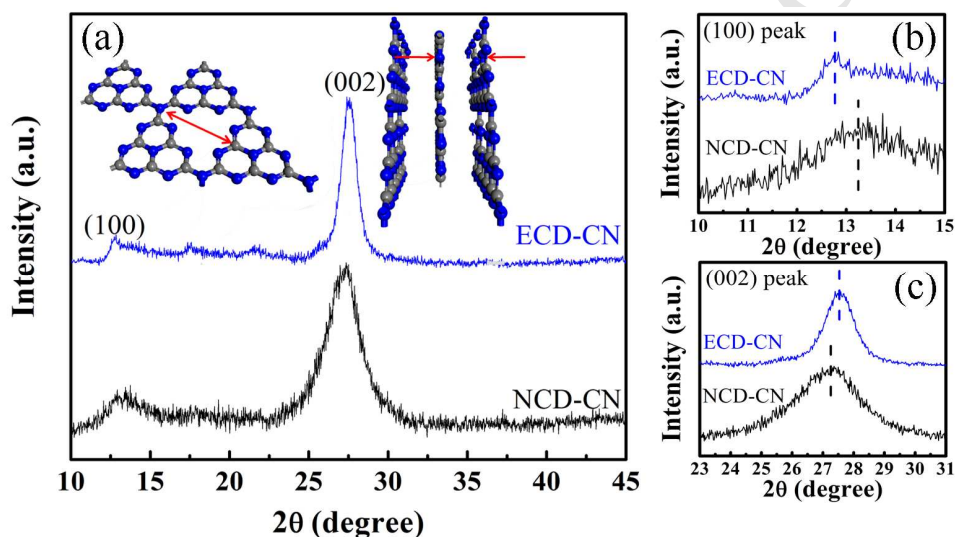


Fig. 1. (a) XRD patterns of g-C₃N₄ samples synthesized in different conditions, and enlarged view of (b) (100) peak and (c) (002) peak.

TEM bright field images of NCD-CN and ECD-CN samples are shown in Fig. 2a and 2c, respectively. The platelet-like morphology can clearly be observed for both two samples, which indicates that the graphitic stacking structure has formed successfully. Further observations on Fig. 2a reveal that the NCD-CN sample is composed of agglomeration of multilayers, resulting in a large thickness. In Fig. 2c, for the ECD-CN sample synthesized in an enclosed ambient atmosphere, the thickness of the flake decreases significantly. Besides, in-plane mesopores of tens of

nanometers are distributed on the g-C₃N₄ nanosheets. AFM was conducted to confirm the thickness evolution of g-C₃N₄ samples synthesized in different conditions. In Fig. S2a, the thickness analysis by AFM reveals that the height of NCD-CN ranges from 10 to 20 nm; whereas, the height of ECD-CN is about 3 nm as shown in Fig. S2b, indicating that the enclosed condition can decrease the thickness of g-C₃N₄ effectively. The thinner mesoporous nanostructures will enlarge the SSA of g-C₃N₄ and reduce the diffusion length of photo-generated carriers, thereby promoting the charge separation during photocatalytic reaction. Fig. 2b and 2d shows the selected area electron diffraction (SAED) patterns of two g-C₃N₄ samples. It displays that both SAED patterns are composed of two diffraction rings corresponding to the (100) and (002) planes of g-C₃N₄, respectively [28], which is consistent with the XRD results. Besides, the ECD-CN sample shows much clearer and sharper polycrystalline diffraction rings than NCD-CN, indicating that the ECD-CN sample has a better crystallization. Simultaneously, TEM images of g-C₃N₄ samples from different precursors were shown in Fig. S3. The dark feature for both D-CN and M-CN samples (Figs. S3a and c) can be attributed to agglomeration of multilayer nanosheets. And from the SAED patterns (Figs. S3b and d), the unclear polycrystalline diffraction rings were observed, indicating that g-C₃N₄ from general method has weak crystallization.

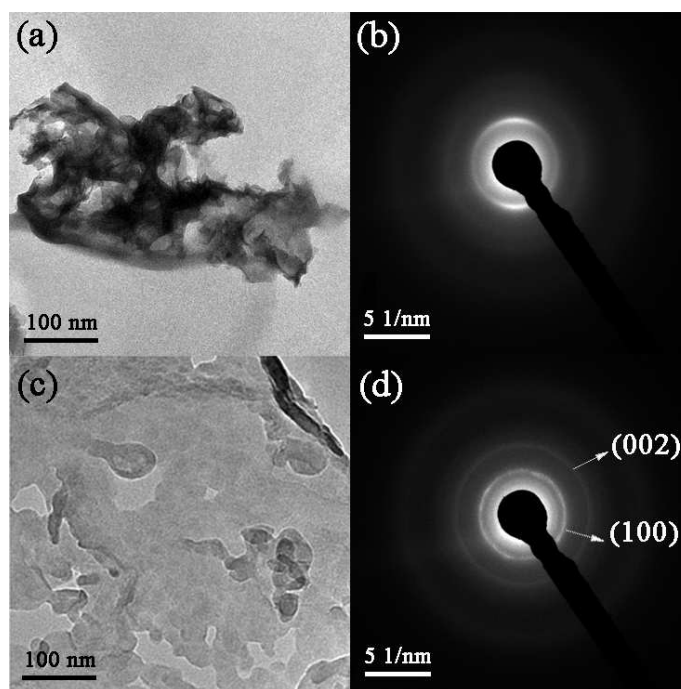


Fig. 2. TEM images and corresponding SAED patterns of (a), (b) NCD-CN and (c), (d) ECD-CN.

XPS was conducted to study the chemical environment and surface stoichiometry. The XPS survey spectra of NCD-CN and ECD-CN in Fig. S4 suggests that there is no other impurity except the C, N and O elements. As shown in Fig. 3a, high resolution C 1s core level for both two samples can be deconvoluted into three components. The peak at 284.6 eV corresponds to the standard reference carbon, the weak one at 286 eV can be attributed to the C-O species because of the incomplete condensation of urea [37-39], and the peak centered at 288.1 eV can be identified as sp^2 -bond carbon ((N-) $_2$ C=N). The N 1s spectrum in Fig. 3b also consists of three parts. The peak located at 398.4 eV corresponds to sp^2 hybridized aromatic N (edge nitrogen atoms) bonded to carbon atoms (C=N-C). The other two peaks at 399.6 eV and 400.7 eV are assigned to the sp^3 hybridized N (including inner nitrogen atoms and bridge nitrogen atoms) bonded to carbon atoms in the form of N-(C) $_3$ and NH $_x$ (NH $_2$ or NH) groups

respectively resulting from the incomplete condensation during the heat treatment, which agrees with the previously reported XPS results [31,40]. The ratio of sp^2 N bonds to the sum of sp^3 N and NH_x is 2.62 for the NCD-CN sample, and 2.76 for the ECD-CN sample (listed in Table 1), respectively, indicating the less defects and better extent of polymerization for the ECD-CN sample [41]. Moreover, sp^2 -bonded nitrogen atom is the principle participant that contributes to band-gap absorption and therefore is an extremely important part of the structure.

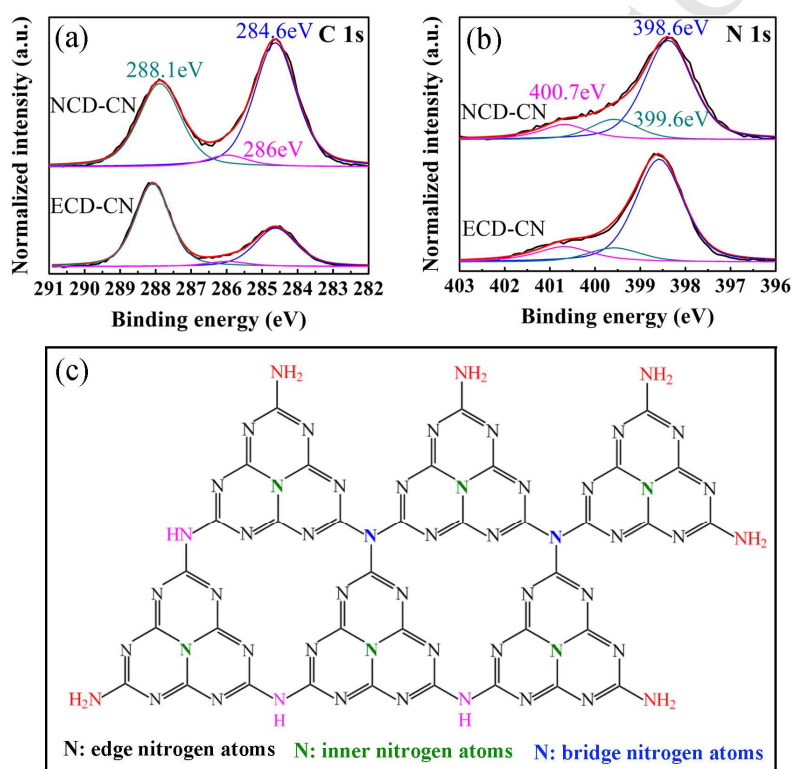


Fig. 3. (a) C 1s and (b) N 1s XPS spectra of NCD-CN and ECD-CN, (c) supercell model of monolayer carbon nitride in a segment with six heptazine units.

Table 1. Relative ratios of bond species of the NCD-CN and ECD-CN samples by N 1s spectral analysis.

N 1s	C-N=C (sp^2)		N-(C) ₃ (sp^3)		NH _x		sp^2 /sum of sp^3 and NH _x
	area	%	area	%	area	%	
NCD-CN	8231.3	72.4	1681.3	14.8	1455.8	12.8	2.62
ECD-CN	15596.6	73.4	2396.6	11.3	3251.1	15.3	2.76

The role of different pyrolysis conditions on the molecular structure of g-C₃N₄ can also be confirmed by FT-IR spectra as depicted in Fig. 4. Both the NCD-CN and ECD-CN samples have the typical patterns of g-C₃N₄. Wherein, the absorption bands at wave number range of 1200-1700 cm⁻¹ are related to the typical stretching modes of CN heterocycles. The broad bands in the range of 3000-3700 cm⁻¹ are indicative of stretching vibration modes for the adsorbed H₂O or residual N-H vibration. The peak at 810 cm⁻¹ is the characteristic breathing mode of the s-triazine ring system, and the one at 888 cm⁻¹ is assigned to deformation mode of N-H [42]. The sharper absorbed bands for the ECD-CN sample are due to the more ordered packing of polymeric melon unit and the enhanced crystallinity [43], which is accordance with the XRD and TEM results discussed above.

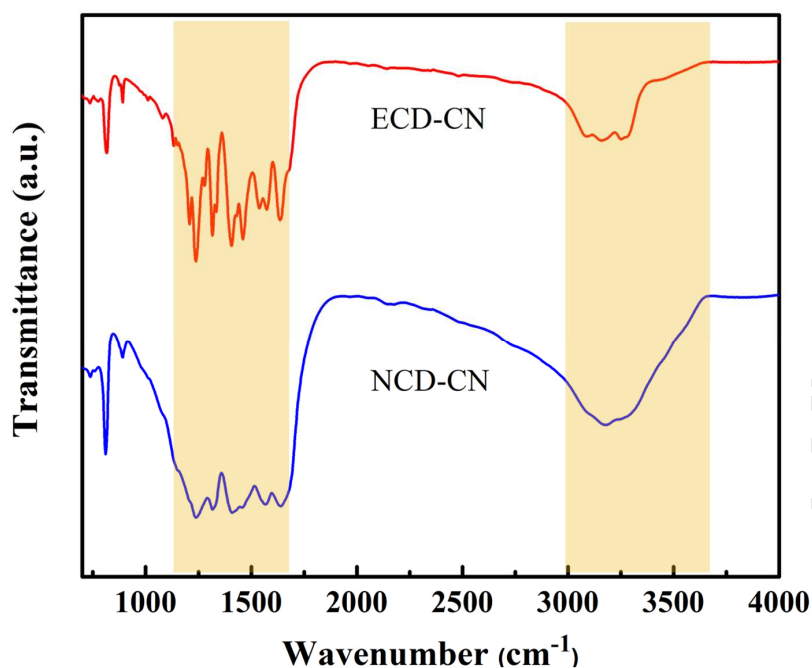


Fig. 4. FT-IR spectra of NCD-CN and ECD-CN.

The specific surface area information on the synthesized $\text{g-C}_3\text{N}_4$ samples was accessed by the nitrogen adsorption-desorption isotherms and Barrett-Joyner-Halenda (BJH) pore-size distribution displayed in Fig. 5 and Table 2. As shown in Fig. 5a, adsorption-desorption isotherms of both two samples are of type IV (BDDT classification), suggesting mesopores exist in $\text{g-C}_3\text{N}_4$. Brunauer-Emmett-Teller (BET) surface area of the ECD-CN sample calculated at a relative pressure range of $p/p_0 = 0.06 - 0.35$ is ca. $141.4 \text{ m}^2 \text{ g}^{-1}$, which is much higher than that of the NCD-CN sample with a SSA of ca. $57.4 \text{ m}^2 \text{ g}^{-1}$. Moreover, the hysteresis loop of the ECD-CN sample shifts to the region of lower relative pressure and the area of hysteresis loop becomes larger compared with the NCD-CN sample, indicating enlarged mesopores formed in ECD-CN sample. For the ECD-CN sample, significant enlargement of the nanopores can also be observed in the pore size distribution curve shown in Fig. 5b. It can be clearly seen that the distribution curve of the ECD-CN

sample is quite broad. Especially, compared with the NCD-CN sample, there is an additional peak corresponding to the pores size of 30 to 60 nm in the curve of the ECD-CN sample. It indicates that the ECD-CN sample has more pores, which makes it have a larger pore volume of $1.014 \text{ cm}^3 \text{ g}^{-1}$ compared with the NCD-CN sample ($0.352 \text{ cm}^3 \text{ g}^{-1}$). The larger pore volume may result from the large number of in-plane holes, as shown in TEM results. From the XPS results (Tables S1 and S2), the relative ratio of lattice carbon atoms ($(\text{N-})_2\text{C}=\text{N}$) to nitrogen atoms is 0.69 for the ECD-CN sample, which is smaller than that of NCD-CN (0.73). This suggests that there are carbon vacancies in ECD-CN and these carbon vacancies may be attributed to the reaction between some carbon species of $\text{g-C}_3\text{N}_4$ with ammonia at high temperature [28], which causes more in-plane pores and in-plane extended distortion in XRD for ECD-CN. Frequently, large SSA and pore volume can make a plenitudinous contact between catalyst and electrolyte and provide abundant active sites, so as to promote the redox reaction and increase transport of charges to reduce the recombination probability of photoexcited carriers. The specific surface area of $\text{g-C}_3\text{N}_4$ from melamine and dicyandiamide precursors were also measured and shown in Fig. S5. The BET surface areas of D-CN and M-CN are $22.6 \text{ m}^2 \text{ g}^{-1}$ and $28.9 \text{ m}^2 \text{ g}^{-1}$, respectively. The pore size distribution curve in Fig. S5b displays that there is a similar additional peak corresponding to the pores size of 30 to 60 nm in the curve of the M-CN sample compared to ECD-CN. However, due to the lower distribution volume of pore, the total pore volumes for D-CN and M-CN are $0.208 \text{ cm}^3 \text{ g}^{-1}$ and $0.278 \text{ cm}^3 \text{ g}^{-1}$, respectively, which is much lower than that of ECD-CN.

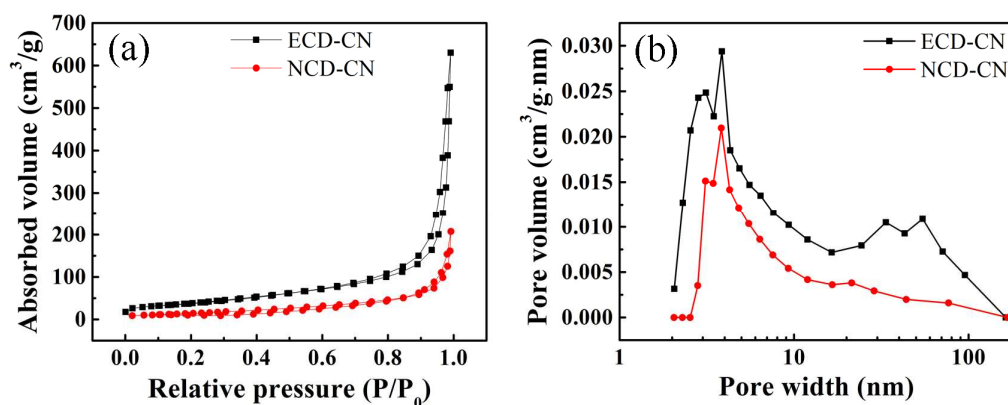


Fig. 5. (a) N_2 adsorption-desorption isotherms of NCD-CN and ECD-CN and (b) the corresponding pore-size distribution curves.

Table 2. Microstructure and photocatalytic properties of $g-C_3N_4$ synthesized in different conditions.

sample	urea ^a (g)	yield ^b (mg)	S_{BET} ^c ($m^2 g^{-1}$)	pore volume ^d ($cm^3 g^{-1}$)	RhB ^e	HER ^f ($\mu mol g^{-1} h^{-1}$)
NCD-CN	10	450	57.4	0.352	45%	131.8
ECD-CN	10	220	141.4	1.014	99%	504.2

^a The mass of urea precursor. ^b The yield of $g-C_3N_4$ at certain mass of urea precursor. ^c BET specific surface area. ^d BJH desorption cumulative volume of pores. ^e Removal percentage of RhB after 10 min photodegradation. ^f Hydrogen production from water splitting.

3.2. Microscopic mechanism of reaction path

To understand the influence of the enclosed condition on structure and morphology

during the pyrolysis and condensation process of urea precursor, a microscopic mechanism of the reaction path of g-C₃N₄ was proposed as shown in Schematic 1 on the basis of the results above and the references.

As shown in Schematic 1, as a precursor of g-C₃N₄, urea contains multiple and complicated reaction steps, and generates many intermediates during the pyrolysis process. Some intermediates are further involved in the reaction and are completely consumed, while some other intermediates including NH₃, H₂O and CO₂ are redundant. Therein, NH₃ gas is the most important component of the pyrolysis-generated atmosphere. On one hand, it is necessary to drive the O elimination process to form the key intermediates at high temperature, which at last polymerize into graphitic carbon nitride. In the enclosed condition, the pyrolysis-generated NH₃ gas doesn't quickly escape the system without further reaction, which makes the less O element residual, and a better polymerization and crystallinity than the NCD-CN sample which have been confirmed by the XRD and TEM results. On the other hand, the redundant NH₃ in the enclosed condition can serve as the etching atmosphere to decompose the bulk g-C₃N₄ and form few-layer and porous nanosheets with large SSA [28,31].

A series of comparison experiments were conducted to confirm the mechanism of the enhanced SSA by preparing g-C₃N₄ samples under different conditions. The preparation conditions and the specific surface areas are listed in Table 3. In the comparison experiments C1 and C2, no g-C₃N₄ can be obtained without the use of a covered crucible, indicating that the initial condensation reaction requires higher local

ammonia concentration. Therefore, it proves that the pyrolysis-generated self-supporting atmosphere (NH_3 gas) is the key factor of converting urea to $\text{g-C}_3\text{N}_4$. In the comparison experiment C3 and C4, 30 mg of NCD-CN samples were annealed at $550\text{ }^\circ\text{C}$ and $450\text{ }^\circ\text{C}$ respectively for 2 h in the tubular furnace, and at the same time, 10 g of urea was placed in the capped crucible in the tubular furnace to react in an enclosed environment, i.e., NCD-CN samples were annealed in the environment of preparation ECD-CN which provides NH_3 . It is found that after the reaction, the annealed NCD-CN samples disappear. Meanwhile, in the comparison experiment C5, the same mass (30 mg) of NCD-CN was annealed at $550\text{ }^\circ\text{C}$ for 2 h in the tubular furnace under non-enclosed environment, i.e., NCD-CN was annealed directly in air without the existence of NH_3 but with the existence of CO_2 . It is interesting that only a small partial mass loss was observed in C5, which may be due to the thermal decomposition effect and can be ignored. C3, C4 and C5 experiments prove that the pyrolysis-generated NH_3 gas plays a key role for continuously etching the $\text{g-C}_3\text{N}_4$ and even making it completely consumed. Besides, C4 experiment excludes the etching effect of H_2O vapor in the present reaction because that the H_2O vapor cannot effectively etch $\text{g-C}_3\text{N}_4$ in such a low temperature of $450\text{ }^\circ\text{C}$ [43]. Moreover, C5 experiment excludes the etching effect of CO_2 in this reaction. In the comparison experiments C6-C8, it shows that the weight of urea does not affect the specific surface area of the final product, which may be because that different weight of urea does not significantly alter the concentration of gas in the tube furnace due to the larger volume and the in-complete seal of tube furnace. In short, it can be concluded

that the pyrolysis-generated NH_3 gas plays an important role in synthesizing $\text{g-C}_3\text{N}_4$ and etching it to provide larger SSA.

Table 3. $\text{g-C}_3\text{N}_4$ synthesized in different experimental conditions.

	reactant	mass	tubular furnace	crucible	other conditions	produced $\text{g-C}_3\text{N}_4$	SSA
C1	urea	10 g	non- enclosed	in crucible without cover	-	No	-
C2	urea	10 g	Enclosed	in crucible without cover	-	No	-
C3	NCD-C N	30 mg	Enclosed	outside the crucible	10 g of urea in the covered crucible, 550 °C	No	-
C4	NCD-C N	30 mg	Enclosed	outside the crucible	10 g of urea in the covered crucible, 450 °C	No	-
C5	NCD-C N	30 mg	Non- enclosed	no	in air	24 mg	-
C6	urea	5 g	Enclosed	in crucible with cover	-	60 mg	141.9 $\text{m}^2 \text{g}^{-1}$
C7	urea	8 g	Enclosed	in crucible	-	205 mg	142.3

				with cover		$\text{m}^2 \text{g}^{-1}$
				in crucible		144.7
C8	urea	20 g	Enclosed	-	166 mg	
				with cover		$\text{m}^2 \text{g}^{-1}$

3.3. Photocatalytic H_2 evolution and photodegradation

The photocatalytic activity was investigated by detecting the H_2 evolution rate from an aqueous solution under visible-light irradiation ($\lambda > 400 \text{ nm}$) using triethanolamine (TEOA) as electron donor. As shown in Fig. 6a, the NCD-CN sample has the H_2 evolution rate of $131.8 \mu\text{mol h}^{-1} \text{g}^{-1}$. In comparison, a remarkably enhanced H_2 evolution rate of $504.2 \mu\text{mol h}^{-1} \text{g}^{-1}$ is achieved for the ECD-CN sample, which is much superior by a factor of 3.8 to the NCD-CN sample. Simultaneously, durability is another criterion for the practical application. It can be clearly seen that there is no obvious attenuation of photocatalytic H_2 evolution rate for both the NCD-CN and ECD-CN samples after 4 recycling runs, which means that the photocatalytic activity of synthesized $\text{g-C}_3\text{N}_4$ samples is sustained.

The photocatalytic activity and stability of the $\text{g-C}_3\text{N}_4$ samples were also investigated by degradation of RhB under visible-light. Clearly seen in Fig. 6b, for the NCD-CN sample, the removal percentage of RhB is only 29.2% and 45.0% in the first 6 min and 10 min, respectively; while, for the ECD-CN sample, 96.1% RhB has been degraded in the first 6 min and 99.0% RhB has been degraded within 10 min, which are much higher than that of the NCD-CN sample. The degradation stability on RhB over the ECD-CN sample was determined by 4 cycling photocatalytic experiments

under the same conditions as shown in Fig. S6. After 4 recycling runs, the ECD-CN sample maintains high photocatalytic activity, indicating that the synthesized g-C₃N₄ sample is stable enough.

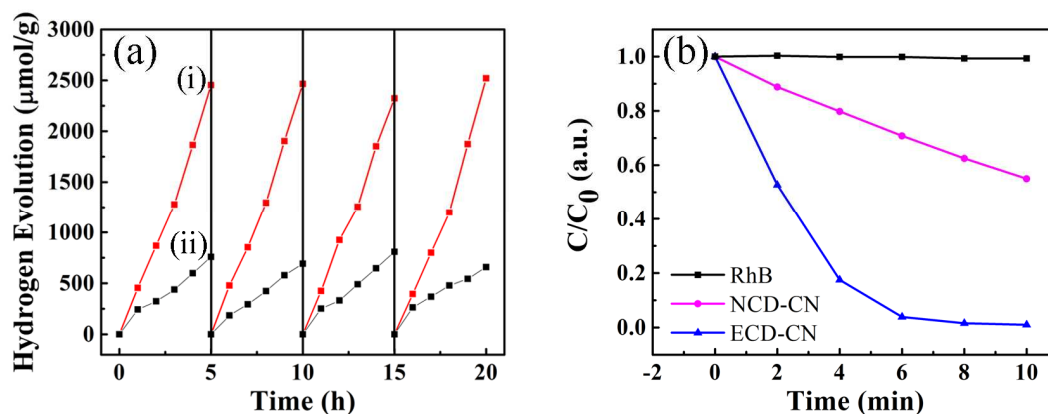


Fig. 6. (a) Photocatalytic H₂ evolution over the g-C₃N₄ samples synthesized under different conditions under visible-light irradiation: (i) ECD-CN, (ii) NCD-CN. (b) The photodegradation of RhB within 10 min under visible-light illumination.

3.4 Band structure and possible photocatalytic mechanism

To depict band structure and photocatalytic mechanism of the g-C₃N₄ samples, the optical and electrochemical properties of g-C₃N₄ samples were conducted. The UV-vis absorption spectra in Fig. 7a presents that the enclosed circumstance leads to a blue shift of absorption edge. The inset of Fig. 7a shows that the ECD-CN sample has shallow color with respect to the NCD-CN sample. The optical band gap of g-C₃N₄ samples can be calculated by Tauc plot method with exponent $r = 2$ as shown in Fig. 7b [44,45]. The obtained band gap (E_g) values are 2.81 eV and 2.94 eV for the NCD-CN sample and the ECD-CN sample, respectively, which are typical values of g-C₃N₄. The increase of band gap of the ECD-CN sample originates from the reduced thickness due to the quantum confinement effect as well as the enhanced structural

connection according to the XRD results [29,46].

Mott-Schottky analysis has been employed to determine the semiconductor type and flat band potential of the g-C₃N₄ samples. The chosen frequencies in the measurement were 1 kHz, 5 kHz and 10 kHz, respectively, and the Mott-Schottky plots of both the NCD-CN and ECD-CN samples are available in Fig. 7c. The donor density is calculated from the slope of the $1/C^2 \sim E$ plot, and the flat band potential is determined by extrapolating it to $C = 0$. It can be seen clearly that the plot slopes are positive for all frequencies, indicating an *n*-type semiconductor behavior for g-C₃N₄ samples. The Mott-Schottky plot of NCD-CN shows a smaller slope than that of ECD-CN, indicating a higher electron donor density for the ECD-CN sample. Higher donor density is helpful for promoting photocatalytic performance because of the increased electrical conductivity and mobility of charges carriers [28]. The flat band potentials are -0.78 eV and -0.87 eV vs NHE for the NCD-CN sample and the ECD-CN sample, respectively. Since the conduction band (CB) potentials of *n*-type semiconductors are very close to the flat band potentials [47], conduction band (CB) and valance band (VB) edge can be deduced on the basis of the flat band potentials and band gap (E_g) values gained from the UV-vis absorption plot, as shown in Fig. 7d. It shows that both NCD-CN and ECD-CN samples satisfy the thermodynamical condition for the photocatalytic splitting of water for hydrogen evolution. Also, The CB edge position of the ECD-CN sample is 0.09 eV higher than that of the NCD-CN sample from the band alignment in Fig. 7d. According to the thermal dynamics principle of photocatalytic water splitting for hydrogen evolution, the ECD-CN has

higher hydrogen evolution ability than the NCD-CN sample, which is consistent with the experimental results.

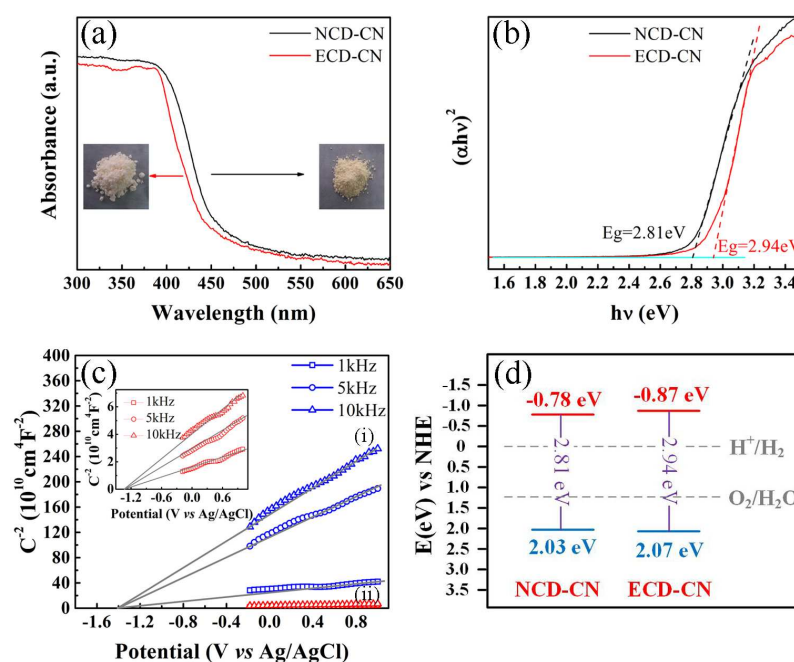


Fig. 7. (a) UV-vis absorption spectra of NCD-CN and ECD-CN. Inset: photographs of g-C₃N₄ grains. (b) Tauc plots of both two samples. The horizontal line marks the baseline; the dashed lines are the tangents of the curves. (c) Mott-Schottky plots of (i) ECD-CN and (ii) NCD-CN collected at various frequencies. The inset of (c) is the magnified view of Mott-Schottky plot of NCD-CN. (d) Band structure of the two samples. The electrolyte is 0.1 M Na₂SO₄ with pH of 5.86.

Electrochemical impedance spectroscopy (EIS) and transient photocurrent measurement were conducted to further study the internal mechanism of enhanced photocatalytic performances of g-C₃N₄ samples. Fig. 8a shows the experimental Nyquist impedance plots of the NCD-CN and ECD-CN samples. Since the semicircle at high frequencies in the Nyquist diagrams is in accordance with the

electron-transfer-limited process and the semicircle diameter is equivalent to the electron-transfer resistance [36], the ECD-CN sample has a more effective separation rate of photo-generated electron-hole pairs and a faster interfacial charge transfer than the NCD-CN sample due to the former has smaller arc radius on EIS Nyquist plot. Besides, it can be obviously seen from Fig. 8b that under visible-light irradiation, the photocurrent density of the ECD-CN sample increases to $3.0 \mu\text{A cm}^{-2}$ with respect to the NCD-CN sample with photocurrent density of $1.2 \mu\text{A cm}^{-2}$. One reason for the enhanced photocurrent density is that the ECD-CN sample has much larger SSA and pore volume than the NCD-CN sample, which increases the amount of the active sites and shortens the diffusion distance of photo-generated electron-hole pairs to promote the separation of the carriers. Besides, better crystallinity with fewer defects, which are always considered as the trap and recombination centers, reduces the recombination of photo-generated carriers for the ECD-CN sample.

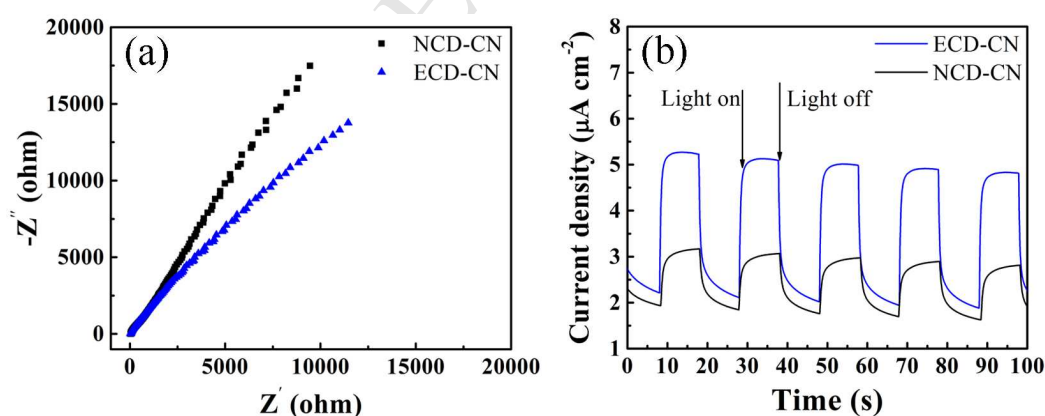


Fig. 8. (a) EIS Nyquist plots. (b) transient photocurrent response of NCD-CN and ECD-CN.

As a result, considering the similar chemical compositions of both the NCD-CN and ECD-CN samples, we provide the responsible factors for the enhanced

photocatalytic activities of the ECD-CN sample. Firstly, the most important factor is that the much higher SSA provides more exposed active sites to the solution for the redox reaction. Meanwhile, the lower thickness shortens the diffusion length, which is beneficial for the rapid transport and separation of the photogenerated carriers to accelerate the photocatalytic reaction in kinetics. Secondly, the ECD-CN sample has a higher CB edge location as well as a lower VB edge location than the NCD-CN sample, displaying a much higher degradation and H₂ evolution capability. Thirdly, the enclosed condition enhances the polymerization and crystallinity and decrease the number of defects of g-C₃N₄, which restrains the recombination of photo-generated carriers, thereby improve the photocatalytic activities.

4. Conclusions

In conclusion, a thin porous g-C₃N₄ with large SSA was prepared using facile one-step method by condensation of urea in an enclosed condition. The generated NH₃ not only self-supports the polymerization of g-C₃N₄ during the pyrolysis process, but also exfoliates the bulk g-C₃N₄ into ultrathin and porous nanosheets producing a high SSA of 141.4 m² g⁻¹, which is appropriate 2.5 times the SSA of the NCD-CN sample. Accordingly, the ECD-CN sample exhibits a much higher photodegradation rate on RhB (99.0% within 10 min) and hydrogen production efficiency (504.2 μmol h⁻¹ g⁻¹) under visible-light due to the more exposed active sites and rapid transport and separation of the photogenerated carriers. Besides, the better polymerization and crystallinity also contribute to the improved photocatalytic activity of the ECD-CN sample. This work can provide a simple approach in designing and preparing an

efficient and sustainable visible-light-driven photocatalyst.

Acknowledgements

This work was supported by the following grants: National Natural Science Foundation of China (No. 51571123, 51671108, 51101088), Tianjin Natural Science Foundation (No. 17JCZDJC37000), and National Basic Research Program of China (973 Program with No. 2014CB931703).

References

- [1] A. Fujishima, K. Honda, Electrochemical photolysis of water at a semiconductor electrode, *Nature* 238(5358) (1972) 37-38.
- [2] G. Liu, L. Wang, H. Yang, H. Cheng, G. Lu, Titania-based photocatalysts-crystal growth, doping and heterostructuring, *J. Mater. Chem.* 20(5) (2010) 831-843.
- [3] D. Zhang, G. Li, J.C. Yu, Inorganic materials for photocatalytic water disinfection, *J. Mater. Chem.* 20(22) (2010) 4529-4536.
- [4] M.D. Hernández-Alonso, F. Fresno, S. Suárez, J.M. Coronado, Development of alternative photocatalysts to TiO_2 : challenges and opportunities, *Energy Environ. Sci.* 2(12) (2009) 1231-1257.
- [5] H. Tong, S. Ouyang, Y. Bi, N. Umezawa, M. Oshikiri, J. Ye, Nano-photocatalytic materials: possibilities and challenges, *Adv. Mater.* 24(2) (2012) 229-251.
- [6] Y.S. Jun, W.H. Hong, M. Antonietti, A. Thomas, Mesoporous, 2D hexagonal carbon nitride and titanium nitride/carbon composites, *Adv. Mater.* 21(42) (2009) 4270-4274.

- [7] A. Thomas, A. Fischer, F. Goettmann, M. Antonietti, J.O. Müller, R. Schlögl, et al., Graphitic carbon nitride materials: variation of structure and morphology and their use as metal-free catalysts, *J. Mater. Chem.* 18(41) (2008) 4893-4908.
- [8] X. Wang, K. Maeda, A. Thomas, K. Takanabe, G. Xin, J.M. Carlsson, et al., A metal-free polymeric photocatalyst for hydrogen production from water under visible light, *Nat. Mater.* 8(1) (2009) 76-80.
- [9] Q. Han, B. Wang, J. Gao, Z. Cheng, Y. Zhao, Z. Zhang, et al., Atomically thin mesoporous nanomesh of graphitic C_3N_4 for high-efficiency photocatalytic hydrogen evolution, *ACS Nano* 10(2) (2016) 2745-2751.
- [10] G. Zhang, Z. Lan, L. Lin, S. Lin, X. Wang, Overall water splitting by Pt/g- C_3N_4 photocatalysts without using sacrificial agents, *Chem. Sci.* 7(5) (2016) 3062-3066.
- [11] X. Wang, K. Maeda, X. Chen, K. Takanabe, K. Domen, Y. Hou, et al., Polymer semiconductors for artificial photosynthesis: hydrogen evolution by mesoporous graphitic carbon nitride with visible light, *J. Am. Chem. Soc.* 131(5) (2009) 1680-1681.
- [12] S. Kumar, T. Surendar, B. Kumar, A. Baruah, V. Shanker, Synthesis of highly efficient and recyclable visible-light responsive mesoporous g- C_3N_4 photocatalyst via facile template-free sonochemical route, *RSC Advances* 4(16) (2014) 8132-8137.
- [13] T. Sano, S. Tsutsui, K. Koike, T. Hirakawa, Y. Teramoto, N. Negishi, et al., Activation of graphitic carbon nitride (g- C_3N_4) by alkaline hydrothermal treatment for photocatalytic NO oxidation in gas phase, *J. Mater. Chem. A* 1(21) (2013)

6489-6496.

- [14] S. Li, Z. Wang, X. Wang, F. Sun, K. Gao, N. Hao, et al., Orientation controlled preparation of nanoporous carbon nitride fibers and related composite for gas sensing under ambient conditions, *Nano Res.* 10(5) (2017) 1710-1719.
- [15] J. Sun, J. Zhang, M. Zhang, M. Antonietti, X. Fu, X. Wang, Bioinspired hollow semiconductor nanospheres as photosynthetic nanoparticles, *Nat. Commun.* 3 (2012) 1139-1145.
- [16] X. Li, J. Zhang, X. Chen, A. Fischer, A. Thomas, M. Antonietti, et al., Condensed graphitic carbon nitride nanorods by nanoconfinement: promotion of crystallinity on photocatalytic conversion, *Chem. Mater.* 23(19) (2011) 4344-4348.
- [17] X. Li, X. Wang, M. Antonietti, Mesoporous g-C₃N₄ nanorods as multifunctional supports of ultrafine metal nanoparticles: hydrogen generation from water and reduction of nitrophenol with tandem catalysis in one step, *Chem. Sci.* 3(6) (2012) 2170-2174.
- [18] M. Hu, J. Reboul, S. Furukawa, L. Radhakrishnan, Y. Zhang, P. Srinivasu, et al., Direct synthesis of nanoporous carbon nitride fibers using Al-based porous coordination polymers (Al-PCPs), *Chem. Commun.* 47(28) (2011) 8124-8126.
- [19] Y. Cui, J. Zhang, G. Zhang, J. Huang, P. Liu, M. Antonietti, et al., Synthesis of bulk and nanoporous carbon nitride polymers from ammonium thiocyanate for photocatalytic hydrogen evolution, *J. Mater. Chem.* 21(34) (2011) 13032-13039.
- [20] Y. Cui, J. Huang, X. Fu, X. Wang, Metal-free photocatalytic degradation of 4-chlorophenol in water by mesoporous carbon nitride semiconductors, *Catal. Sci.*

- Technol. 2(7) (2012) 1396-1402.
- [21] J. Zhang, F. Guo, X. Wang, An optimized and general synthetic strategy for fabrication of polymeric carbon nitride nanoarchitectures, *Adv. Funct. Mater.* 23(23) (2013) 3008-3014.
- [22] X. Zou, G. Li, Y. Wang, J. Zhao, C. Yan, M. Guo, et al., Direct conversion of urea into graphitic carbon nitride over mesoporous TiO₂ spheres under mild condition, *Chem. Commun.* 47(3) (2011) 1066-1068.
- [23] H. Yan, Soft-templating synthesis of mesoporous graphitic carbon nitride with enhanced photocatalytic H₂ evolution under visible light, *Chem. Commun.* 48(28) (2012) 3430-3432.
- [24] J. Xu, Y. Wang, Y. Zhu, Nanoporous graphitic carbon nitride with enhanced photocatalytic performance, *Langmuir* 29(33) (2013) 10566-10572.
- [25] X. Chen, Y. Jun, K. Takanabe, K. Maeda, K. Domen, X. Fu, et al., Ordered mesoporous SBA-15 type graphitic carbon nitride: a semiconductor host structure for photocatalytic hydrogen evolution with visible light, *Chem. Mater.* 21(18) (2009) 4093-4095.
- [26] H. Xu, J. Yan, X. She, L. Xu, J. Xia, Y. Xu, et al., Graphene-analogue carbon nitride: novel exfoliation synthesis and its application in photocatalysis and photoelectrochemical selective detection of trace amount of Cu²⁺, *Nanoscale* 6(3) (2014) 1406-1415.
- [27] Y. Li, R. Jin, Y. Xing, J. Li, S. Song, X. Liu, et al., Macroscopic foam-like holey ultrathin g-C₃N₄ nanosheets for drastic improvement of visible-light

- photocatalytic activity, *Adv. Energy Mater.* 6(24) (2016) 1601273-1601277.
- [28] Q. Liang, Z. Li, Z. Huang, F. Kang, Q. Yang, Holey graphitic carbon nitride nanosheets with carbon vacancies for highly improved photocatalytic hydrogen production, *Adv. Funct. Mater.* 25(44) (2015) 6885-6892.
- [29] G. Liu, P. Niu, C. Sun, S.C. Smith, Z. Chen, G. Lu, et al., Unique electronic structure induced high photoreactivity of sulfur-doped graphitic C_3N_4 , *J. Am. Chem. Soc.* 132(33) (2010) 11642-11648.
- [30] Y. Kang, Y. Yang, L. Yin, X. Kang, G. Liu, H. Cheng, An amorphous carbon nitride photocatalyst with greatly extended visible-light-responsive range for photocatalytic hydrogen generation, *Adv. Mater.* 27(31) (2015) 4572-4577.
- [31] P. Yang, J. Zhao, W. Qiao, L. Li, Z. Zhu, Ammonia-induced robust photocatalytic hydrogen evolution of graphitic carbon nitride, *Nanoscale* 7(45) (2015) 18887-18890.
- [32] J. Liu, T. Zhang, Z. Wang, G. Dawson, W. Chen, Simple pyrolysis of urea into graphitic carbon nitride with recyclable adsorption and photocatalytic activity, *J. Mater. Chem.* 21(38) (2011) 14398-14401.
- [33] S. Ma, S. Zhan, Y. Jia, Q. Shi, Q. Zhou, Enhanced disinfection application of Ag-modified g- C_3N_4 composite under visible light, *Appl. Catal. B: Environ.* 186(5) (2016) 77-87.
- [34] P. Wu, J. Wang, J. Zhao, L. Guo, F.E. Osterloh, Structure defects in g- C_3N_4 limit visible light driven hydrogen evolution and photovoltage, *J. Mater. Chem. A* 2(47) (2014) 20338-20344.

- [35] F. Dong, Z. Wang, Y. Sun, W. Ho, H. Zhang, Engineering the nanoarchitecture and texture of polymeric carbon nitride semiconductor for enhanced visible light photocatalytic activity, *J. Colloid Interface Sci.* 401 (2013) 70-79.
- [36] X. She, L. Liu, H. Ji, Z. Mo, Y. Li, L. Huang, et al., Template-free synthesis of 2D porous ultrathin nonmetal-doped g-C₃N₄ nanosheets with highly efficient photocatalytic H₂ evolution from water under visible light, *Appl. Catal. B* 187 (2016) 144-153.
- [37] Y. Zhao, F. Zhao, X. Wang, C. Xu, Z. Zhang, G. Shi, et al., Graphitic carbon nitride nanoribbons: grapheme-assisted formation and synergic function for highly efficient hydrogen evolution, *Angew. Chem. Int. Edit.* 53(50) (2014) 13934-13939.
- [38] J. Liang, Y. Zheng, J. Chen, J. Liu, D. Hulicova-Jurcakova, M. Jaroniec, et al., Facile oxygen reduction on a three-dimensionally ordered macroporous graphitic C₃N₄/carbon composite electrocatalyst, *Angew. Chem. Int. Edit.* 124(16) (2012) 3958-3962.
- [39] H. Yu, L. Shang, T. Bian, R. Shi, G. I. N. Waterhouse, Y. Zhao, et al., Nitrogen-doped porous carbon nanosheets templated from g-C₃N₄ as metal-free electrocatalysts for efficient oxygen reduction reaction, *Adv. Mater.* 28(25) (2016) 5080-5086.
- [40] J. Duan, S. Chen, M. Jaroniec, S. Qiao, Porous C₃N₄ nanolayers@N-graphene films as catalyst electrodes for highly efficient hydrogen evolution, *ACS nano* 9(1) (2015) 931-940.

- [41] D.J. Martin, K. Qiu, S.A. Shevlin, A.D. Handoko, X. Chen, Z. Guo, et al., Highly efficient photocatalytic H₂ evolution from water using visible light and structure-controlled graphitic carbon nitride, *Angew. Chem. Int. Edit.* 53(35) (2014) 9240-9245.
- [42] C. Ye, J. Li, Z. Li, X. Li, X. Fan, L. Zhang, et al., Enhanced driving force and charge separation efficiency of protonated g-C₃N₄ for photocatalytic O₂ evolution, *ACS Catal.* 5(11) (2015) 6973-6979.
- [43] P. Yang, H. Ou, Y. Fang, X. Wang, A facile steam reforming strategy to delaminate layered carbon nitride semiconductors for photoredox catalysis, *Angew. Chem. Int. Ed.* 129(14) (2017) 4050-4054.
- [44] J. Liu, Y. Liu, N. Liu, Y. Han, X. Zhang, H. Huang, et al., Metal-free efficient photocatalyst for stable visible water splitting via a two-electron pathway, *Science* 347(6225) (2015) 970-974.
- [45] K. Schwinghammer, M.B. Mesch, V. Duppel, C. Ziegler, J. Senker, B.V. Lotsch, Crystalline carbon nitride nanosheets for improved visible-light hydrogen evolution, *J. Am. Chem. Soc.* 136(5) (2014) 1730-1733.
- [46] J. Zhang, M. Zhang, G. Zhang, X. Wang, Synthesis of carbon nitride semiconductors in sulfur flux for water photoredox catalysis, *ACS Catal.* 2(6) (2012) 940-948.
- [47] L. Li, J. Yan, T. Wang, Z. Zhao, J. Zhang, J. Gong, et al., Sub-10 nm rutile titanium dioxide nanoparticles for efficient visible-light-driven photocatalytic hydrogen production, *Nat. Commun.* 6 (2014) 5881-5891.